

Zero- and one-dimensional magnetic traps for quasi-particles

P. Redliński,¹ T. Wojtowicz,^{1,2} T. G. Rappoport,³ A. Libál,¹ J. K. Furdyna,¹ and B. Jankó¹

¹*Department of Physics, University of Notre Dame, Notre Dame, IN 46556*

²*Institute of Physics, Polish Academy of Sciences, 02-668 Warsaw, Poland*

³*Instituto de Física, Universidade Federal do Rio de Janeiro,
Cx. P 88528, 21945-970 Rio de Janeiro RJ, Brazil*

We investigate the possibility of trapping quasi-particles possessing spin degree of freedom in hybrid structures. The hybrid system we are considering here is composed of a semi-magnetic quantum well placed a few nanometers below a ferromagnetic micromagnet. We are interested in two different micromagnet shapes: cylindrical (micro-disk) and rectangular geometry. We show that in the case of a micro-disk, the spin object is localized in all three directions and therefore zero-dimensional states are created, and in the case of an elongated rectangular micromagnet, the quasi-particles can move freely in one direction, hence one-dimensional states are formed. After calculating profiles of the magnetic field produced by the micromagnets, we analyze in detail the possible light absorption spectrum for different micromagnet thicknesses, and different distances between the micromagnet and the semimagnetic quantum well. We find that the discrete spectrum of the localized states can be detected via spatially-resolved low temperature optical measurement.

I. INTRODUCTION

Currently, there is an increasing interest in using the spin of particles, in addition to their charge, as the basis for new types of electronic devices^{1,2,3}. In this work we show by theoretical calculations that the spin degree of freedom can be utilized for achieving spatial localization - of interest for "spintronic applications" - of charged quasi-particles (electrons, holes or trions^{4,5}), as well as of neutral complexes, such as excitons^{4,6}.

In this paper we consider a hybrid structure consisting of a CdMnTe/CdMgTe quantum well (QW) structure at a small, but finite distance from ferromagnetic micromagnet. Due to the Zeeman interaction, the non-homogeneous magnetic field produced by the micromagnet acts as an effective potential that can "trap" spin polarized quasi-particles in the QW. In this article we explore two specific types of micromagnets: one with a cylindrical⁷, and one with a rectangular^{8,9,10} symmetry. In both cases the thickness of the micromagnets is of order of a few hundreds of nanometers and their lateral dimension is of order of microns. We will show that in both geometries, micromagnets are very effective in localizing quasi-particles. For the micro-disk, the quasi-particles are localized below the center of the disk in all three spatial directions; and for the rectangular micromagnet, the quasi-particles are localized below the poles of the ferromagnet and the localization occurs only in two spatial dimensions. Thus in the latter case the quasi-particles can move quasi-freely in one direction.

The choice of diluted magnetic semiconductor (CdMnTe) QW instead of the classical one (e.g. CdTe) is motivated by perspective of achieving the more efficient spin traps, leading to the clear localization effects. In diluted magnetic semiconductor (DMS) materials the exchange interaction between delocalized band electrons and localized magnetic ions (Mn⁺⁺ ions in the case at hand), leads to a splitting between band states for different spin components (for a review of relevant properties of DMS see Ref. [11]). The so-called giant Zeeman spin splitting has been extensively investigated in the 80's in II-VI based DMSs¹² and because of this effect the effective g -factor for the DMS is very high. For example, Dietl¹³ *et al.* reported an electron g -factor of about 500 in a sub-Kelvin experiment in a CdMnSe, which implies a value of about 2000 for the g -factor of a hole in this material. According to our previous estimations¹⁰ such values for the effective g -factors can in fact result in the confinement of quasi-particles in a small lateral region inside QW. The actual details of the optical response will depend in sensitive way on the values of the electron and hole g -factors.

Our focus on QW structures instead of normal films has both experimental and theoretical motivations. From the experimental point of view, we would like to avoid the complications caused by the metal-DMS interface. To satisfy that criterion, the QW should be placed at a finite distance from the micromagnet. The local magnetic field inside the QW diminishes as the distance d between the micromagnet and the QW increases. Thus, we need some compromise for the value of d in order to have a high magnetic field in the QW, and at the same time to avoid interface contamination effects. There are also two theoretical motivations that require the QW to be relatively narrow. First, because of the quantum confinement, the heavy and light hole states that are degenerate in the bulk at the Γ point become non-degenerate in the QW geometry. This means that the low-energy absorption spectrum is simplified for the QW. Second, in the narrow QW we can assume that the local magnetic field is

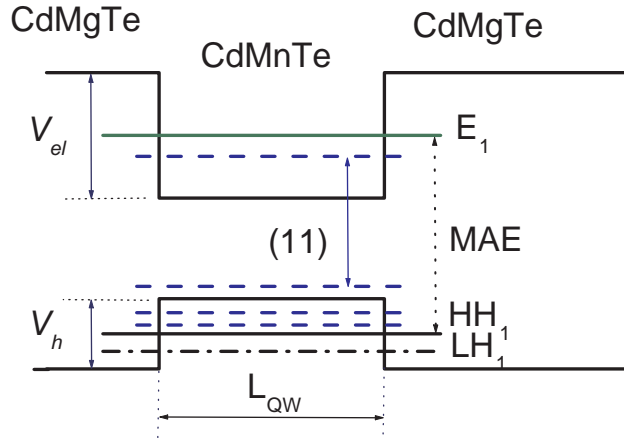


FIG. 1: In the absence of a micromagnet we expect the main absorption edge (MAE) between HH_1 and E_1 energy states (full lines). Both energy states are two-fold-degenerate without external magnetic field. After the deposition of the micromagnet, new states appear below the E_1 state and above the HH_1 state (dashed lines). Each new energy state is *non-degenerate*. In a QW structure the heavy hole states and the light hole states, e.g., HH_1 and LH_1 , are split even without external magnetic field.

uniform throughout the width of the QW which again simplifies the calculation. On the other hand, for practical reasons the QW cannot be too narrow, since the line width of the optical resonances increases¹⁴ with decreasing width of the QW (L_{QW}).

In Fig. 1 we present a schematic sketch of the energy states in a DMS QW which can be used for discussing the presence of ferromagnetic micromagnet on the top of the quantum structure. The QW is grown in the (001) direction, chosen here as the \hat{z} axis. Without the micromagnet, the main absorption edge is observed between the states of the heavy hole HH_1 (with a pseudo spin of $-3/2$) and the electron E_1 (with a spin of $-1/2$) in the σ_+ circularly polarized light. In the absence of magnetic field E_1 and HH_1 are two-fold degenerate with respect to the spin, and the first optical transition in the σ_- polarization is at the same energy as for the σ_+ transition. After depositing the micromagnet, we expect that new states will appear below E_1 and above HH_1 . These new states are non-degenerate, since the presence of a local magnetic field lifts the Kramers degeneracy. It is important to note that the spin of the states below E_1 remains $-1/2$, and above HH_1 states remains with their pseudo-spin of $-3/2$. Our main prediction is the following: the experimentally observable transitions between these new states will appear in the absorption or photoluminescence spectrum below the main absorption edge, and will obey selection rules for σ_+ circularly polarized light¹⁵. We will specifically analyze optical absorption, because it provides a mapping of all states; but our results are equally well suited for photoluminescence experiments if only the ground state is of interest.

This paper is organized as follows: In the next section we present the general theoretical approach used and the approximations made. Then we analyze theoretically the g-factor anisotropy of the hole states. In section III A we show the results obtained for the absorption coefficient of the micro-disk/QW structure as a function of key parameters; and in section III B we present the analysis for the rectangular ferromagnetic micromagnet/QW hybrid. In the last section we present a detailed discussion and their consequences.

II. THEORETICAL APPROACH

The goal of this section is to derive effective Hamiltonians for both geometries of micromagnet which can be treated numerically but which possess all important properties of the original problem. We begin this section by considering separately the electron in the valence- and in the conduction band. We then discuss the Zeeman

interaction between the local magnetic field produced by micromagnet and the quasi-particle spin. At the end of this section we discuss the experimentally observed anisotropy of the hole g-factor (g_h).

We begin with the Luttinger Hamiltonian¹⁶ H_L of the valence electron in the k-representation (note that we are working in the *electron* representation of the valence band), within the base of the four-component spinor $\Psi^\dagger = (\Psi_{+3/2}^*, \Psi_{-1/2}^*, \Psi_{+1/2}^*, \Psi_{-3/2}^*)$,

$$H_L = \begin{pmatrix} H^a & H^b \\ H^{b*} & {}^T H^a \end{pmatrix}, \quad (1)$$

where the matrices H^a and H^b (of rank two) can be written schematically as

$$H^a = \begin{pmatrix} H_h & -c \\ -c & H_l \end{pmatrix}, \quad (2)$$

$$H^b = \begin{pmatrix} -b & 0 \\ 0 & b \end{pmatrix}, \quad (3)$$

and where $c = -\frac{\hbar^2}{2m_0}\sqrt{3}(\gamma_2(k_x^2 - k_y^2) - 2i\gamma_3k_xk_y)$, $b = -\frac{\hbar^2}{2m_0}2\sqrt{3}\gamma_3k_z(k_x - ik_y)$. The symbol ${}^T H^a$ denotes the H^a matrix with interchanged *diagonal* elements. Please note that b is proportional to k_z a property we will use later in the discussion. The OX, OY and OZ axis correspond to [1,0,0], [0,1,0] and [0,0,1] crystallographic directions and the spin is quantized along [0,0,1]. Using the substitution $\vec{k} \Rightarrow -i\vec{\nabla}$, the Hamiltonian in the \vec{k} -representation is transformed to the \vec{r} -representation.

Now we consider the QW structure. We choose our 4-component spinor wave function in the following form:

$$\Psi(\vec{r}) = \begin{pmatrix} \Psi_{3/2}(\vec{r}) \\ \Psi_{-1/2}(\vec{r}) \\ \Psi_{1/2}(\vec{r}) \\ \Psi_{-3/2}(\vec{r}) \end{pmatrix} = \begin{pmatrix} f_h(z)\phi_{+\frac{3}{2}}(x, y) \\ f_l(z)\phi_{-\frac{1}{2}}(x, y) \\ f_l(z)\phi_{+\frac{1}{2}}(x, y) \\ f_h(z)\phi_{-\frac{3}{2}}(x, y) \end{pmatrix}, \quad (4)$$

where $\phi(x, y)$'s are not yet determined, and $f_h(z)$ and $f_l(z)$ are ground state functions of the following set of two Schrödinger eigen-equations,

$$\left(\frac{\hbar^2(\gamma_1 - 2\gamma_2)}{2m_0} \frac{d^2}{dz^2} + V_{QW}^h(z) \right) f_h(z) = \epsilon_h f_h(z), \quad (5)$$

$$\left(\frac{\hbar^2(\gamma_1 + 2\gamma_2)}{2m_0} \frac{d^2}{dz^2} + V_{QW}^h(z) \right) f_l(z) = \epsilon_l f_l(z). \quad (6)$$

where ϵ_h, ϵ_l are the ground state energies. In Eqs. (5) and (6) $m_0/(\gamma_1 - 2\gamma_2)$ and $m_0/(\gamma_1 + 2\gamma_2)$ are the heavy- and light hole masses in the z-direction and $V_{QW}^h(z)$ is a potential energy of the QW coming from discontinuity of the edge of the valence band. We assume this potential to be rectangular (see Fig. 1),

$$V_{QW}^h(z) = \begin{cases} 0 & \text{for } |z| < L_{QW}/2 \\ -V_h & \text{for } |z| > L_{QW}/2. \end{cases} \quad (7)$$

The functions $f_h(z)$ and $f_l(z)$ which satisfy Eqs. (5) and (6) are real-valued even functions fulfilling the relation $\int f_h^*(z) p_z f_l(z) dz = 0$. These properties of f_h and f_l can be used as follows: In the subspace of Hilbert space spanned by our trial wave function, H_L Eq. (1) is written as a new 4x4 matrix \tilde{H}_L ,

$$\tilde{H}_L = \begin{pmatrix} \tilde{H}^a & \tilde{H}^b \\ \tilde{H}^b & {}^T \tilde{H}^a \end{pmatrix}, \quad (8)$$

where

$$\tilde{H}^a = \begin{pmatrix} H_h & -c \cdot I_{hl} \\ -c \cdot I_{hl}^* & H_l \end{pmatrix}, \quad (9)$$

and

$$\tilde{H}^b = \begin{pmatrix} 0 & 0 \\ 0 & 0 \end{pmatrix}. \quad (10)$$

Symbol I_{hl} in Eq. (9) is the overlap integral, defined by $I_{hl} \equiv \int f_h^*(z) f_l(z) dz$. Furthermore, in the \vec{r} -representation the two quantities H_h and H_l in the matrix \tilde{H}^a take the following form:

$$H_h = \frac{\hbar^2}{2m_0}(\gamma_1 + \gamma_2) \left(\frac{d^2}{dx^2} + \frac{d^2}{dy^2} \right) + \epsilon_h, \quad (11)$$

$$H_l = \frac{\hbar^2}{2m_0}(\gamma_1 - \gamma_2) \left(\frac{d^2}{dx^2} + \frac{d^2}{dy^2} \right) + \epsilon_l, \quad (12)$$

$$-c = -\frac{\hbar^2}{2m_0}\sqrt{3} \left(\gamma_2 \left(\frac{d^2}{dx^2} - \frac{d^2}{dy^2} \right) - 2i\gamma_3 \frac{d}{dx} \frac{d}{dy} \right).$$

After making these approximations the wave function $\tilde{\Psi}$ satisfying $\tilde{H}_L \tilde{\Psi} = E_h \tilde{\Psi}$ has only two non-vanishing components,

$$\tilde{\Psi}(\vec{r}) = \begin{pmatrix} \phi_{+\frac{3}{2}}(x, y) \\ \phi_{-\frac{1}{2}}(x, y) \\ 0 \\ 0 \end{pmatrix}, \quad (13)$$

and

$$\tilde{\Psi}(\vec{r}) = \begin{pmatrix} 0 \\ 0 \\ \phi_{+\frac{1}{2}}(x, y) \\ \phi_{-\frac{3}{2}}(x, y) \end{pmatrix}. \quad (14)$$

The Zeeman interaction due to the local magnetic field produced by the micromagnet mixes both states and lifts their degeneracies.

Now we consider the conduction band. We assume that the dispersion relation of the conduction electron is parabolic, its Hamiltonian H_e taking the form

$$H_e = E_G - \frac{\hbar^2}{2m_0}\gamma_{el} \left(\frac{d^2}{dx^2} + \frac{d^2}{dy^2} + \frac{d^2}{dz^2} \right) + V_{QW}^{el}(z), \quad (15)$$

where E_G is the energy gap of a QW, m_0/γ_{el} is the electron effective mass, and V_{QW}^{el} is the potential energy coming from the discontinuity of the conduction band (see Fig. 1):

$$V_{QW}^{el}(z) = \begin{cases} 0 & \text{for } |z| < L_{QW}/2 \\ V_{el} & \text{for } |z| > L_{QW}/2 \end{cases}. \quad (16)$$

For the electron we assume the following factorized trial wave function

$$\Psi_{el} = \begin{pmatrix} f_{el}(z)\phi_+(x, y) \\ f_{el}(z)\phi_-(x, y) \end{pmatrix}, \quad (17)$$

where the function $f_{el}(z)$ is the solution of the one-dimensional Schrödinger equation

$$\left(-\frac{\hbar^2\gamma_{el}}{2m_0} \frac{d^2}{dz^2} + V_{QW}^{el}(z) \right) f_{el}(z) = \epsilon_{el} f_{el}(z). \quad (18)$$

Both functions ϕ_{\pm} fulfill the following eigen-equation

$$\tilde{H}_e \phi_{\pm}(x, y) \equiv \left(-\frac{\hbar^2\gamma_{el}}{2m_0} \left(\frac{d^2}{dx^2} + \frac{d^2}{dy^2} \right) + \epsilon_{el} \right) \phi_{\pm}(x, y) = E_e \phi_{\pm}(x, y). \quad (19)$$

The Zeeman Hamiltonian used for both the conduction and the valence electrons can be written as

$$H_Z(\vec{r}) = \mu_B \vec{s} \hat{g}_{eff} \vec{B}(\vec{r}), \quad (20)$$

where \hat{g}_{eff} is a tensor, μ_B is the Bohr magneton, $\vec{B}(\vec{r})$ is the local magnetic field produced by the micromagnet, and \vec{s} is the spin- $\frac{1}{2}$ operator. For the conduction band $\hat{g}_{eff} = g_e \hat{1} \equiv \text{diag}(g_e, g_e, g_e)$ and for valence electron $\hat{g}_{eff} = g_h \hat{1} \equiv \text{diag}(g_h, g_h, g_h)$, where $\hat{1}$ is the 3x3 identity matrix. For the conduction electron, the spin- $\frac{1}{2}$ operator in the basis of the Bloch states is a 2x2-matrix proportional to the Pauli matrices. For the valence electron the spin operator is a 4x4-matrix, as shown in Ref. [17]. In addition to the previous approximations we assume that the QW is narrow, and we rewrite Eq. (20) as

$$\tilde{H}_Z(x, y) = \mu_B \vec{s} \hat{g}_{eff} \vec{B}(x, y, z = d), \quad (21)$$

where d is the distance between the QW and the micromagnet.

Original Hamiltonians are transformed into the 2D effective Hamiltonians because of the form of the trial wave function we used. The total effective Hamiltonians of the valence (\mathcal{H}_h) and of the conduction electron (\mathcal{H}_e) then become

$$\mathcal{H}_h(x, y) = \tilde{H}_L(x, y) + \tilde{H}_Z(x, y), \quad (22)$$

$$\mathcal{H}_e(x, y) = \tilde{H}_e(x, y) + \tilde{H}_Z(x, y). \quad (23)$$

The procedure of the calculation is as follows: first, the magnetic field produced by the micromagnet is calculated by solving the magneto-static Maxwell equations¹⁸, either by using a magnetization distribution determined from micromagnetic simulations⁷ in the case of the disk or by assuming that the micromagnet can be represented by a uniformly magnetized domain in the case of rectangular micromagnet. Then, the electronic spectrum of the conduction band and the valence band is calculated by approximating the Schrödinger eigen-equations with finite difference algebraic equations. In the case of the micro-disk, the finite difference equations are generated on a two-dimensional grid and Eqs. (22), (23) are solved directly. In the case of the rectangular micromagnet - because of its large elongation in the y-direction ($D_y=2\mu\text{m}$) - we can make the ansatz that the quasi-particle is free to move in this direction so the plane wave form of the wave function is assumed in y-direction. Thus, in the case of a rectangular micromagnet the finite difference equations are generated only on a one-dimensional grid.

Given the calculated eigen-values and eigen-functions, we use the Fermi's Golden rule to obtain the absorption coefficient¹⁵

$$\alpha_{\pm}(\omega) \simeq \frac{1}{\omega} \sum_{i,j} | \langle e_j | p_x \pm i p_y | h_i \rangle |^2 \delta(\hbar\omega - (E_{e_i} - E_{h_i})), \quad (24)$$

where $\{|e_i \rangle, E_{e_i}\}$ and $\{|h_j \rangle, E_{h_j}\}$ are the eigen-solutions of the conduction and valence band Hamiltonians, \mathcal{H}_e and \mathcal{H}_h , respectively. The Coulomb interaction between the electrons and the holes leads to the creation of long-lived excitons, which in turn generate sharp individual optical lines. We assumed that the exciton states are formed and that the MAE corresponds to the 1S exciton transition in the QW without the micromagnet. In the following figures we have taken the zero energy at the 1S exciton main absorption peak. To create the final spectrum, each optical line which we calculate is broadened by a gaussian function with a linewidth of 1 meV. This is a reasonable approximation for typical experimental resolution.

A. Anisotropy of the g-factor of the hole

The Zeeman splitting of the valence band edge depends on the direction of the magnetic field with respect to the growth direction of the quantum well¹⁹. In order to demonstrate this we consider two configurations: a constant magnetic field parallel to the plane of the quantum well, $\vec{B} = B\vec{e}_x$; and a constant magnetic field perpendicular to this plane, $\vec{B} = B\vec{e}_z$.

Starting with $\vec{B} = B\vec{e}_z$, we find it convenient to use a different basis than that used in the previous part of the paper: the new basis vectors are $\Psi^\dagger = (\Psi_{+3/2}^*, \Psi_{-3/2}^*, \Psi_{+1/2}^*, \Psi_{-1/2}^*)$. In this new basis, the Luttinger Hamiltonian, Eq. (1) or Eq. (8), for the edge of the valence band in the QW is a diagonal matrix

$$H = \begin{pmatrix} +\frac{1}{2}g_h\mu_B B & 0 & 0 & 0 \\ 0 & -\frac{1}{2}g_h\mu_B B & 0 & 0 \\ 0 & 0 & -\Delta_{lh} + \frac{1}{6}g_h\mu_B B & 0 \\ 0 & 0 & 0 & -\Delta_{lh} - \frac{1}{6}g_h\mu_B B \end{pmatrix}, \quad (25)$$

where the energy splitting $\Delta_{lh} = |E_l - E_h|$ is caused by the quantum well confinement. This splitting is also present in structures under strain and it can be either positive or negative as shown in Ref. 17. Looking at the Hamiltonian H , Eq. (25), we can see that the energy of the heavy hole ($+\frac{3}{2}, -\frac{3}{2}$) splits by $|g_h\mu_B B|$, whereas the energy of the light hole ($+\frac{1}{2}, -\frac{1}{2}$) splits by $|\frac{1}{3}g_h\mu_B B|$, an amount smaller by a factor of 3.

In order to analyze the second geometry ($\vec{B} = B\vec{e}_x$), we write the Hamiltonian for the valence band edge in a QW as follows:

$$H = \begin{pmatrix} \mathbf{0} & \mathbf{0} & \frac{1}{2\sqrt{3}}g_h\mu_B B & 0 \\ \mathbf{0} & \mathbf{0} & 0 & \frac{1}{2\sqrt{3}}g_h\mu_B B \\ \frac{1}{2\sqrt{3}}g_h\mu_B B & 0 & -\Delta_{lh} & \frac{1}{3}g_h\mu_B B \\ 0 & \frac{1}{2\sqrt{3}}g_h\mu_B B & \frac{1}{3}g_h\mu_B B & -\Delta_{lh} \end{pmatrix}. \quad (26)$$

If we omit the mixing between the heavy and light holes (i.e., if we retain only the bold elements in Eq. (26)) then the heavy holes do not split, and the light holes split by $|\frac{2}{3}g_h\mu_B B|$. We note that the light hole splitting is now two times larger than in the case of the perpendicular magnetic field, $\vec{B} = B\vec{e}_z$, where it was $|\frac{1}{3}g_h\mu_B B|$. Solving eigenvalue problem with Hamiltonian H , Eq. (26), we obtain four solutions as a function of the external magnetic field (see Fig. 2):

$$E_h^\mp = -\frac{\Delta_{lh}}{2} \mp \frac{g_h\mu_B B}{6} + \frac{1}{6}\sqrt{9\Delta_{lh}^2 \pm 6\Delta_{lh}g_h\mu_B B + 4(g_h\mu_B B)^2}, \quad (27)$$

$$E_l^\mp = -\frac{\Delta_{lh}}{2} \mp \frac{g_h\mu_B B}{6} - \frac{1}{6}\sqrt{9\Delta_{lh}^2 \pm 6\Delta_{lh}g_h\mu_B B + 4(g_h\mu_B B)^2}. \quad (28)$$

When the QW splitting $\Delta_{lh} \gg |g_h\mu_B B|$ then up to terms quadratic in the external field B , Eqs. (27) and (28) can be further simplified to

$$E_h^\mp \approx \frac{1}{12} \frac{g_h\mu_B B}{\Delta_{lh}} g_h\mu_B B, \quad (29)$$

$$E_l^\mp \approx -\Delta_{lh} \mp \frac{g_h\mu_B B}{3} - \frac{1}{12} \frac{g_h\mu_B B}{\Delta_{lh}} g_h\mu_B B. \quad (30)$$

Because the heavy hole does not split, we are left with 3 solutions out of the 4. In this approximation the energy level of the heavy hole E_h^\mp is twofold degenerate and the light hole splits by an amount proportional to the magnetic field ($\frac{2}{3}|\mu_B g_h B|$), as seen in Eq. (30). These different behaviors can be compared in Fig. 2 where we plotted exact values of E_h^\pm and E_l^\mp using Eqs. (27) and (28).

In other words, we can say that in a QW, the g_h -factor of the first heavy hole states HH_1 is highly anisotropic. Consequently, in the Zeeman term given by Eqs. (20) or (21), the tensor $\hat{g}_h = \text{diag}(g_h, g_h, g_h)$ can be approximated by $\hat{g}_h \approx \text{diag}(0, 0, g_h)$. Indeed, only the component of the field parallel to the growth direction of the QW splits the HH_1 states. The anisotropy that appears naturally using the Luttinger Hamiltonian in the QW is observed experimentally¹⁹. We compared the results of the optical response for both isotropic and anisotropic g -factors, and found that absorption spectra are similar, especially in the low-energy region of the spectrum. This result is presented in the next paragraph.

III. RESULTS AND DISCUSSION

For the calculations involving both cylindrical and rectangular micromagnets, the following set of Luttinger parameters and electron mass was chosen for both the QW and the barriers: $\gamma_1=4.14$, $\gamma_2=1.09$, $\gamma_3=1.62$,

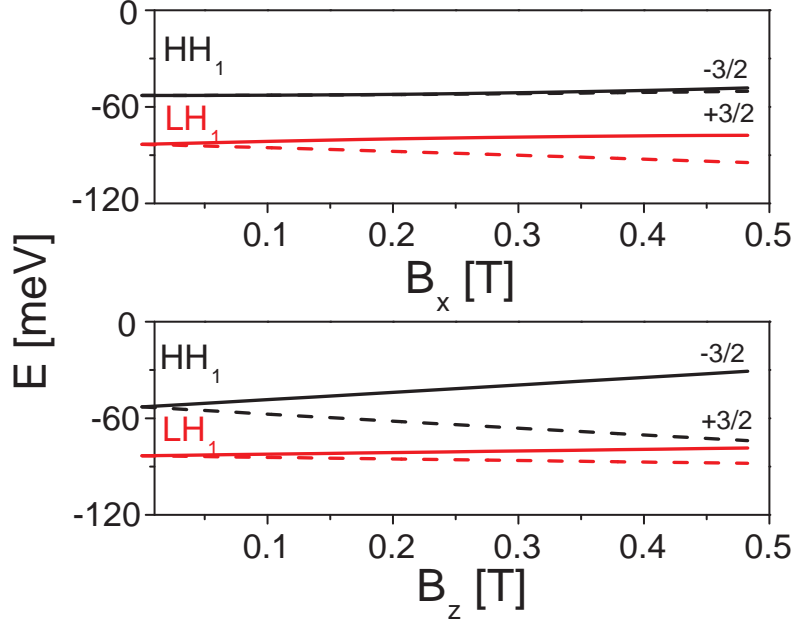


FIG. 2: Top panel: splitting of the heavy hole (HH_1) and light hole (LH_1) edges at the Γ point in a QW vs. B_x (we use the electron representation). B_y and B_z are set to zero. Bottom panel: splitting of the heavy hole and light hole edges in a QW vs. B_z ($B_x=0$ and $B_y=0$). Solid and dashed lines represent states with opposite spin. Heavy hole states $\mp 3/2$ do not split when the magnetic field is applied in the plane of the QW as seen on the upper panel.

$m_e = m_0/\gamma_e = 0.096 m_0$. From Eq. (12), the heavy hole effective mass in the plane is $m_0/(\gamma_1 + \gamma_2) = 0.19 m_0$ and light hole effective mass in the plane $m_0/(\gamma_1 - \gamma_2) = 0.33 m_0$. A total discontinuity of bands $V_T = 500$ meV, and valence band offset $vbo = 0.4$ is assumed, which corresponds to a discontinuity in the valence band of $V_h = V_T vbo = 200$ meV, and a discontinuity in the conduction band of $V_{el} = V_T \cdot (1 - vbo) = 300$ meV (see Fig. 1). We also choose a quantum well width of $L_{QW} = 20$ Å, for which the splitting between the heavy hole HH_1 and the light hole LH_1 energy states is $\Delta_{lh} \approx 50$ meV. Note that there is only one bound heavy hole state and only one bound light hole state for these parameters.

A. Cylindrical micromagnet: a zero-dimensional trap

We investigate a Fe micro-disk (with a diameter of $R = 1$ μm , a thickness $D_z = 50$ nm, and $\mu_0 M_s = 2.2$ T) in the vortex state^{7,20}. In this state, due to the competition between the exchange energy and the demagnetization energy, the magnetization lies in the plane of the micro-disk except near the center, where the local magnetization points out of the plane (to reduce the exchange energy), and forms a magnetic vortex. The diameter of the core (R_c) to which the non-zero perpendicular magnetization is confined extends over only about 60 nm, as previously calculated⁷. It is important to mention that only the z-component M_z of the total magnetization \vec{M} produces the "spike" in the magnetic field \vec{B} which traps the quasi-particles.

Having magnetization profile of the vortex^{7,20} and using magneto-static Maxwell equation magnetic field \vec{B} is calculated. In Fig. 3 we show the distribution of the magnetic field $\vec{B}(x, y, d)$ in the XY plane at a distance d above the micromagnet, where d is the separation between the micromagnet and the QW. In the magnetostatic picture, the magnetic field \vec{B} is produced by two magnetic charges (of diameter R_c) on two surfaces of the micromagnet. These magnetic charges are separated by a thickness of the micromagnet, D_z . At a distance $d = 10$ nm above the

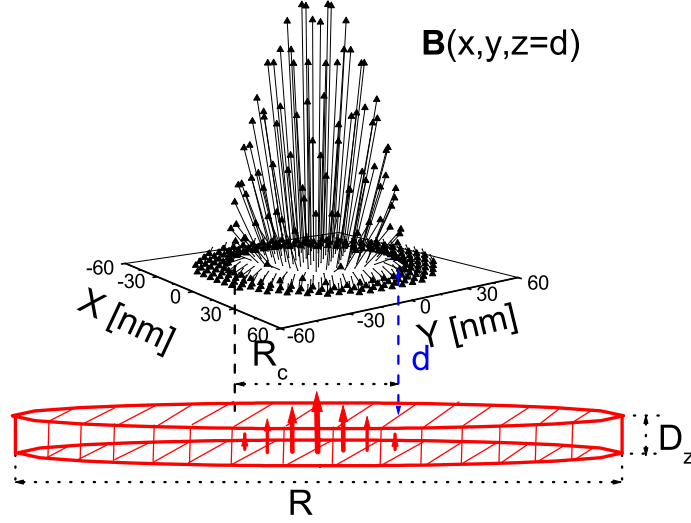


FIG. 3: Three-dimensional image of a magnetic field $B(x, y, z = d)$ on the XY surface at a distance d above Fe micro-disk. It is assumed that micromagnet is in a vortex state. The diameter of the region where the z-component of the magnetization M_z is non-zero (the core region) is only of the order of $R_c = 60$ nm, whereas the diameter of the micro-disk R is $1 \mu\text{m}$, and the thickness of the disk D_z is 50 nm. M_z depicted by vertical arrows in the core region is very well approximated by a parabolic profile.

micromagnet, the maximum value of the magnetic field is $|\vec{B}|_{max} = 0.46$ T. The field is nonzero over a distance of 60 to 80 nm from the center of the disk, as shown in Fig. 3. Such a strongly localized magnetic field in both x and y directions, together with the QW confinement results in a quasi-particle localization in all three directions. The particle is localized below the center of the micro-disk. We will refer to this system as a zero-dimensional trap.

In Fig. 4 we show the absorption coefficient for three distances d between the micro-disk and the QW: $d=5$ nm, 10 nm and 15 nm. The energy of the photon is measured relative to the energy of the main absorption peak in the QW in the absence of a micromagnet (see Fig. 1). Vertical bars represent the optical oscillator strength of the transitions, and the numbers $(n_c n_v)$ show that the corresponding line is a transition between the n_v^{th} hole state and the n_c^{th} electron state. Eigenenergies of the conduction electron fulfil $E_1 < E_2 < \dots < E_{n_c} < \dots$ and E_1 is the ground state of the conduction band electron. Eigenenergies of the valence electron fulfil $E_1 > E_2 > \dots > E_{n_v} > \dots$ and E_1 is the ground state of the valence band electron.

The absorption line was obtained after broadening the δ -distribution of each transition, Eq. (24), with a Gaussian function (the line width of each resonance is $w=1$ meV). As expected, the peaks shift to lower energies with decreasing d , as the maximum value of B , and thus the effective 'potential', are larger for smaller d . At $d=10$ nm, the shift between the (11) transition and the main absorption peak is around 25 meV (we will call this quantity the *binding energy*). As is seen in Fig. 4, the first transition (11) is the most intense, but we can see that non-diagonal transitions (14),... also have a relatively large spectral weight. We also see that for a set of parameters we used in calculation the two closely lying lines (22) and (33) merge into a single large peak in the absorption spectrum.

In Fig. 5 we show the absorption coefficient for two different thicknesses D_z of the micro-disk and a value of d fixed at 10 nm. When the thickness D_z increases from 50 nm to 150 nm, the binding energy increases from 25 meV to 28 meV. Transition (51), not seen for $d=10$ nm in Fig. 4, now becomes visible at $D_z=150$ nm. On the other hand, increasing D_z to larger values does not change the absorption substantially, because the separation

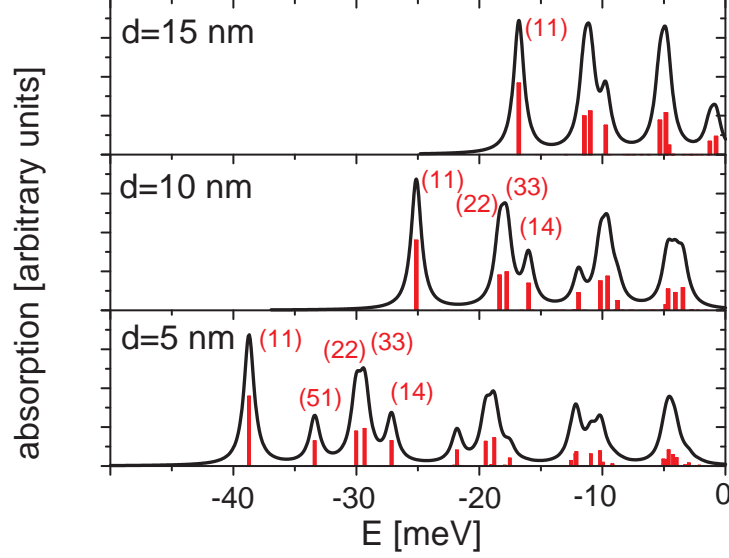


FIG. 4: Absorption coefficient for three distances d between the micro-disk and the QW with $D_z=50$ nm. The number $(n_c n_v)$ corresponds to transitions between the n_c^{th} electron state and the n_v^{th} hole state.

between magnetic charges (D_z) begins to exceed the dimension of the magnetic charge (R_c).

To get further insight into the optical transitions we follow the prescription defined in Ref. 7 and write the conduction electron two component spinor as

$$\psi_{m,k}^c = f_{el}(z) e^{im\phi} \begin{pmatrix} e^{-i\phi} g_{m,k}^{\uparrow}(\rho) \\ g_{m,k}^{\downarrow}(\rho) \end{pmatrix}, \quad (31)$$

where $m=0, \pm 1, \pm 2, \dots$ is the angular momentum quantum number, $k=0, 1, 2, \dots$ is the radial quantum number and we used cylindrical coordinates (ρ, ϕ, z) . This form of the angular dependence of the wave function is exact for electrons described by spherically symmetric bands with quadratic dispersion. Assuming that the valence band can also be approximated by a quadratic dispersion, the hole four-component spinor has the following form

$$\psi_{m,k}^v = e^{im\phi} \begin{pmatrix} f_h(z) e^{-3i\phi} g_{m,k}^{+3/2}(\rho) \\ f_l(z) e^{-2i\phi} g_{m,k}^{+1/2}(\rho) \\ f_l(z) e^{-i\phi} g_{m,k}^{-1/2}(\rho) \\ f_h(z) g_{m,k}^{-3/2}(\rho) \end{pmatrix}. \quad (32)$$

The dominant part of the electron and the hole wave function calculated in our approach is of the form given in Eqs. (31) and (32).

In Ref. 7 the intra-band optical transitions of the conduction band were studied. Selection rules for this type of the transitions imply that the angular momentum quantum number of the envelope wave function m must be changed by ± 1 in σ_{\pm} polarizations ($\Delta m = \pm 1$). On the other hand for inter-band transitions $\Delta m = 0$ because the initial and the final Bloch states are of different symmetry: the initial state is of P symmetry and the final state is of S symmetry. In order to calculate the σ_+ absorption coefficient using Eq. (24) we have to calculate two integrals: $\langle \Psi_{-3/2} | \Psi_{\downarrow} \rangle$ and $\langle \Psi_{-1/2} | \Psi_{\uparrow} \rangle$. Using Eqs. (31) and (32) as an approximation for the true wave function we have

$$\langle \Psi_{-3/2} | \Psi_{\downarrow} \rangle \approx \int e^{-im\phi} (f_h(z) g_{m,k}^{-3/2}(\rho))^* f_{el}(z) e^{im'\phi} g_{m',k'}^{\downarrow}(\rho) d\phi r dr dz \sim \delta_{m,m'},$$

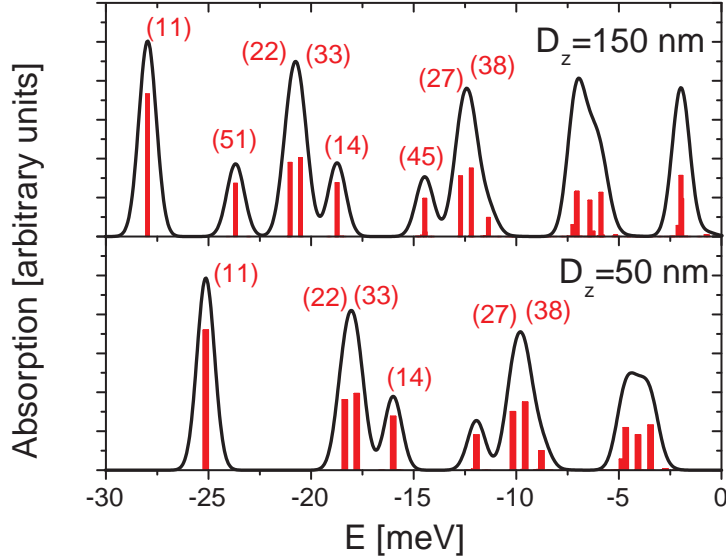


FIG. 5: Absorption coefficient for two thicknesses D_z of the ferromagnetic micro-disk. In magnetostatic language, D_z is the distance between magnetic charges. The separation between the micro-disk and the QW was set to $d=10$ nm.

TABLE I: Mapping of the quantum number n that was used in Fig. 4 and Fig. 5 to described hole states on the (m,k) pairs. Only four states, $n=1,4$, which fulfill $E_1 > E_2 > E_3 > E_4$ are mapped, and E_1 is the ground state of the electron in the valence band.

n_v	m	k
1	0	0
2	-1	0
3	+1	0
4	0	1

$$\langle \Psi_{-1/2} | \Psi_{\uparrow} \rangle \approx \int e^{-im\phi} (f_h(z) g_{m,k}^{-1/2}(\rho))^* f_{el}(z) e^{im'\phi} g_{m',k'}^{\uparrow}(\rho) d\phi r dr dz \sim \delta_{m,m'},$$

from where the conservation of the m number is immediately obtained: $m = m'$.

In Tab. I we show the mapping between the notation of the hole states used previously n_v and the (m, k) notation. A similar table can be drawn for the electron states. As an example, the non-diagonal optical transition (14) shown both in Fig. 4 or Fig. 5 is relatively strong because both the first electron state (1) and the fourth hole state (4) have the same m quantum number, i.e. $m = 0$.

B. Rectangular micromagnet: a one-dimensional trap

In this section we consider a rectangular, flat Fe micromagnet in the single domain state¹⁸, with magnetization pointing in the x -direction^{9,21}, see also Ref. 10. The single-domain state of the micromagnet with the mentioned size was investigated by micro-magnetic simulation using the OOMMF package²². Without an external magnetic field the sample does not remain as an ordered single-domain, but rather goes into a multi-domain structure. The simulation shows however, that after magnetizing the sample with a field of 1 T and reducing the field close to 0 T, a value of 0.2 T is sufficient to restore a state that - for our purposes - is sufficiently close to a single

domain. Because of the magnetic anisotropy of the g_h , this additional field is unimportant for electrons in the valence band, but it does have a slight effect on the conduction electron spectrum.

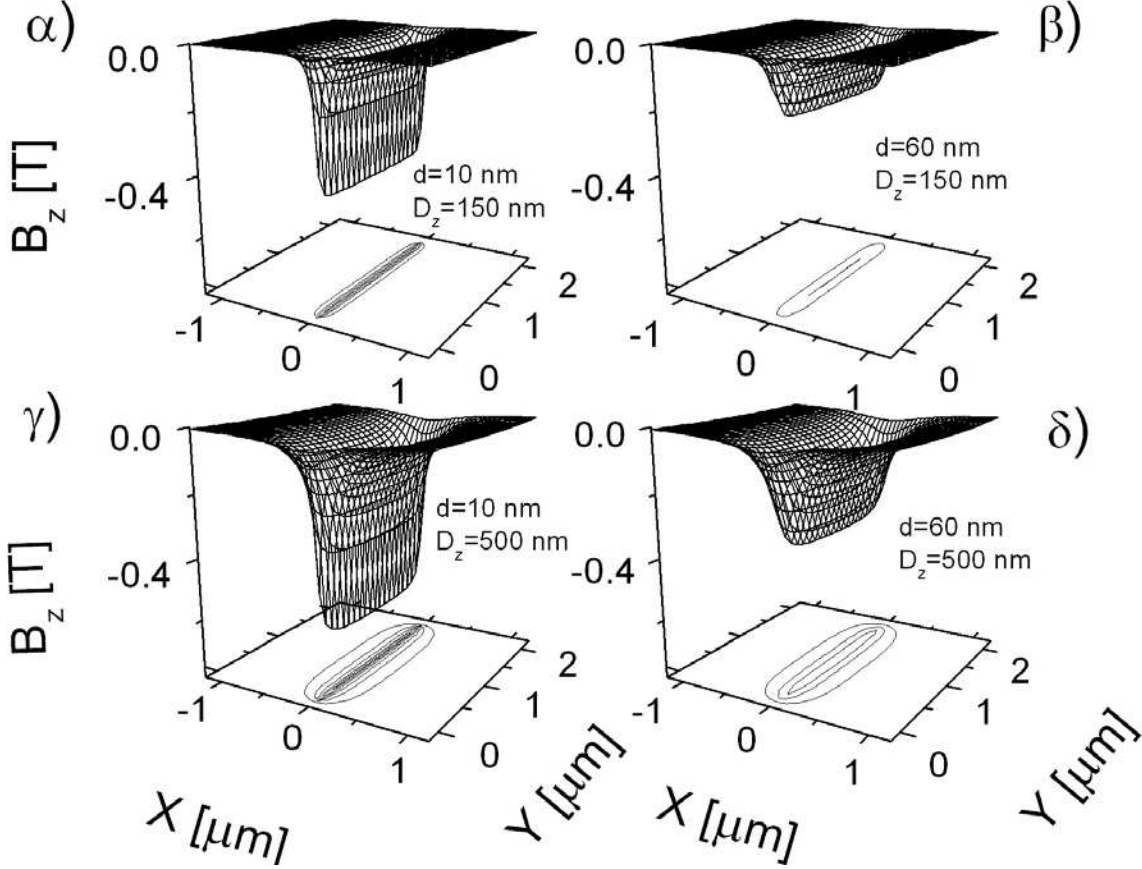


FIG. 6: Z-component of the magnetic field \vec{B} produced by a rectangular micromagnet at a distance d below its narrow edge. We show results for two distances $d=10$ nm, $d=60$ nm and for two micromagnet thicknesses, $D_z=150$ nm and $D_z=500$ nm. Contour plots on the XY planes indicate localization and 'strength' of the z-component of the magnetic field.

In Fig. 6 we present the z-component of the magnetic field below one of the two poles of the micromagnet ($D_x=6 \mu\text{m} \times D_y=2 \mu\text{m} \times D_z$, see inset in Fig. 7). The thickness D_z is a parameter in our simulations, and we vary this value in the range from 150 to 500 nm. For large D_x , the local magnetic field $\vec{B}(\vec{r})$ can be thought to be a sum of two fields (one of them is shown in Fig. 6) produced by the magnetic charges localized at the two magnetic poles of the micromagnet. The magnetic field B_z on the second pole has an opposite direction to this field, and thus 'attracts' quasi-particles with the opposite spin. The top two plots (α and β) in Fig. 6 are for two different distances $d=10$ nm, $d=60$ nm keeping a constant thickness of $D_z=150$ nm. The two bottom plots (γ and δ) are for the same distances, using $D_z=500$ nm. When the distance d is increased while keeping the thickness D_z constant (as we go from α to β or from γ to δ), the magnetic field B_z is seen to decrease, as expected. In contrast, when the thickness D_z increases for a constant d ($\alpha \rightarrow \gamma$ or $\beta \rightarrow \delta$), the magnetic field B_z is seen to increase. This suggests that, by depositing thicker micromagnets, larger magnetic fields can be produced for the same separation between the micromagnet and the QW. In Fig. 6, we also show contour plots of B_z on the XY plane, which indicate the spatial extent of the magnetic field and its gradient. In all cases (α , β , γ and δ), we see that B_z is confined to a narrow region in the x-direction, and is delocalized in the y-direction over the distance of two microns. With increasing thickness D_z ($\alpha \rightarrow \gamma$ or $\beta \rightarrow \delta$) the "spread" of B_z in the x-direction is seen to increase.

Our calculations show that at $d=10$ nm ($D_z=150$ nm), the maximum value of the magnetic field is $|\vec{B}|_{max}=0.6$ T. This value is larger than for a micro-disk because in the present case the thickness of the rectangular micromagnet is larger. We must emphasize that the gradient of the magnetic field²³ is as large as 2 mT/Å for $d=10$ nm, so

that a precise determination of $|\vec{B}|_{max}$ or of the magnetic field profile is challenging even in the simple case of a single-domain phase.

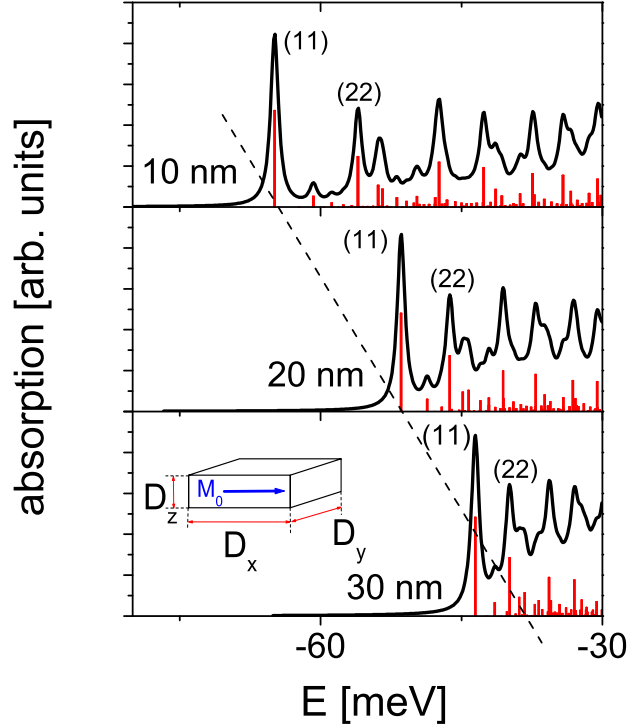


FIG. 7: Absorption coefficient for three distances $d=10, 20$ and 30 nm (from top to bottom) between the rectangular micromagnet ($D_z=150$ nm, $D_x=6\mu\text{m}$ and $D_y=2\mu\text{m}$) and the QW. The binding energy as well as the separation between the peaks decreases almost linearly with increasing d . In the inset we show the arrangement of the rectangular micromagnet in a single domain state. Magnetization is pointing in the x -direction.

In Fig. 7 we present the absorption spectrum at three distances d between the QW and the micromagnet: $d=10, 20$, and 30 nm. In all three cases thickness of the micromagnet was kept at a constant value of $D_z=150$ nm. As before, zero energy is chosen at the main absorption peak. At $d=10$ nm, the binding energy is 66 meV, while at $d=60$ nm it is smaller by a factor of 2. This follows from the fact that the further the micromagnet is from the QW, the smaller is the magnetic field at the QW position (see also Fig. 6). Non-diagonal transitions are relatively strong both in the case of the micro-disk and of the rectangular micromagnet¹⁰. The separation between the peaks decreases as d increases, because the gradient of the magnetic field (and equivalently, the gradient of the potential) also decreases with increasing d .

In Fig. 8 we show the behavior of the absorption coefficient for three thicknesses $D_z=100, 200$, and 300 nm, for the same micromagnet-QW distance d . With increasing D_z , the binding energy increases almost linearly. This is seen in Fig. 8 as a linear shift of the (11) transition. An interesting observation is that the separation between the peaks does not depend on D_z in the range $100-300$ nm and for the parameters which we have used. As in the previous paragraphs the pair $(n_c n_v)$ denotes transition between the n_v^{th} hole state and the n_c^{th} electron state. Contrary to the disk case, for the rectangular micro-magnet only (odd, odd) or (even, even) transitions are allowed, see Fig 9.

Let us now return to the anisotropy of the g -factor of the holes that was described in the theoretical part of this paper. In Fig. 9 we compare the absorption spectrum calculated for the two approximations: the isotropic and the anisotropic cases of the g_h -factor. As an example we have chosen the rectangular micromagnet for discussing the magnetic anisotropy of the QW. The electron g -factor is isotropic in both cases. We see that, at least in the low energy region, the two spectra are the same: the position of the transition energies as well as the oscillator strengths are nearly the same for both g -factor models. Thus, for the arrangement discussed in this work (see inset in Fig. 7) and for the geometrical parameters we have used (such as the size and the shape of the magnets),

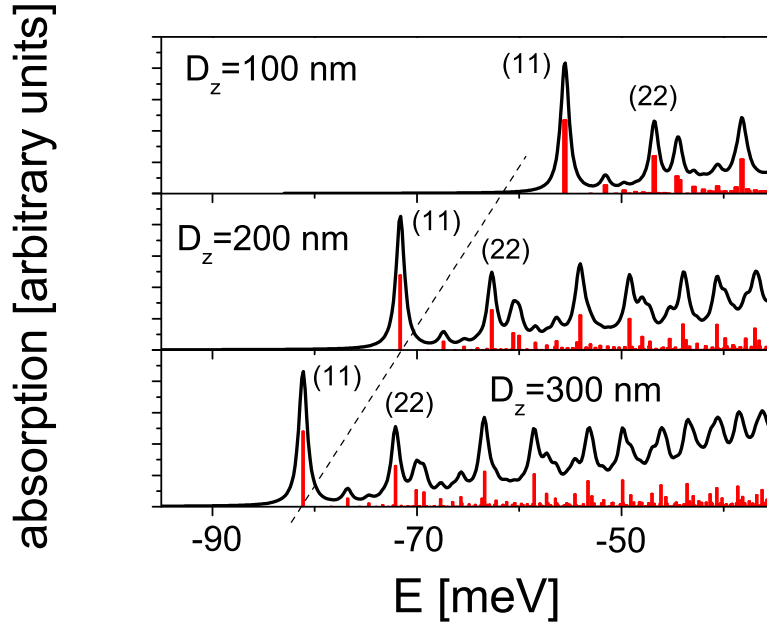


FIG. 8: Absorption coefficient for different thicknesses D_z of a rectangular micromagnet. In this case the distance between the micromagnet and the QW is constant, $d=10$ nm. Separation between peaks is barely distinguishable for all three D_z values. Note that the absorption peak (11) shifts almost linearly with D_z .

only the z-component of the magnetic field produced by the micromagnet is important.

IV. CONCLUSIONS

We analyzed theoretically the optical response of a hybrid structure composed of a micromagnet deposited on top of a diluted magnetic semiconductor quantum well structure. We specifically analyzed the absorption coefficient which is directly related to the optical absorption experiment, but the results of this paper are equally well suited for photoluminescence experiment if only the ground state is of interest.

The calculations were performed for two types of ferromagnetic micromagnets: a cylindrical micro-disk and a rectangular micromagnet. We analyzed the local magnetic field produced by the micromagnets. In the case of a micro-disk this field, together with the QW confinement potential, traps the quasi-particle (e.g., an exciton) in all three spatial directions. However, a rectangular micromagnet traps quasi-particles only in two spatial directions, allowing it to behave as a one-dimensional quasi-particle. We described the approximations we used in our approach, including a discussion of the anisotropy of the g-factor of the hole states. Then we calculated the absorption coefficients for both shapes of the micromagnets for various micromagnet-QW separations and micromagnet thicknesses.

In order to observe zero-dimensional and one-dimensional states inside the DMS QW it is necessary to produce as strong a local magnetic field as possible. This can be achieved, for example, by utilizing materials with high saturation magnetization. Our analysis shows that it is better to deposit a thicker ferromagnetic layer, since thicker micromagnets produce a stronger local magnetic field. As was expected, the growth of a high quality QW relatively close to the ferromagnetic/semiconductor interface is of major importance for optimal quasi-particle localization. Since high values of g-factors are of critical importance for fabricating efficient spin traps, optical localization is most likely expected to be observed in DMS-based quantum structures at low temperature.

Finally, since quasi one-dimensional states emerge only below the poles of the rectangular micromagnet and zero-dimensional states emerge only below the center of the disk, spatially-resolved techniques such as micro-photoluminescence, micro-reflectance or near-field scanning optical microscopy are preferred for observing the

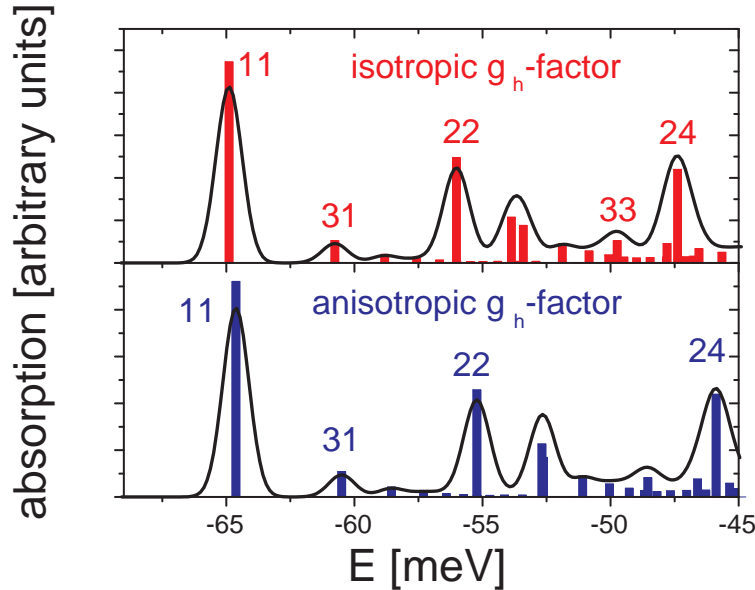


FIG. 9: Comparison of the absorption spectrum in two models: the isotropic and the anisotropic g -factor of the hole. The electron g -factor is isotropic. The top and bottom spectra are very similar. Calculations done for rectangular Fe micromagnet with dimensions of $D_x=6\mu\text{m}$, $D_y=2\mu\text{m}$, $D_z=0.15\mu\text{m}$ on the top of a QW structure at a distance $d=10$ nm apart.

effects presented in this paper. Since both zero- and one-dimensional states are spin polarized, for unambiguous identification of the confined states the use of polarization sensitive techniques are required. Specifically, in the case of a rectangular micromagnet the states created underneath opposite poles should have opposite spin-polarization which can serve as a convincing test of the appearance of these new states.

¹ H. Ohno, F. Matsukura, and Y. Ohno, Japan Society of Applied Physics **5**, 4 (2002).

² D. Grundler, T. M. Hengstmann, and H. Rolff, Brazilian Journal of Physics **34**, 598 (2004).

³ S. Kreuzer, M. Rahm, J. Biggerger, R. Pulwey, J. Raabe, D. Schuh, W. Wegscheider, and D. Weiss, Physica E **16**, 137 (2003).

⁴ P. Kossacki, J. Cibert, D. Ferrand, Y. Merle d'Aubigné, A. Arnoult, A. Wasiela, S. Tatarenko, and J. A. Gaj, Phys. Rev. B **60**, 16018 (1999).

⁵ M. Combescot, O. Betbeder-Matibet, and F. Dubin, European Physical Journal B **42**, 63 (2004).

⁶ J. A. K. Freire, F. M. Peeters, A. Matulis, V. N. Freire, and G. A. Farias, Phys. Rev. B **62**, 7316 (2000).

⁷ M. Berciu and B. Jankó, Phys. Rev. Lett. **90**, 246804 (2003).

⁸ J. Kossut, I. Yamakawa, A. Nakamura, G. Cywiński, K. Fronc, M. Czczcott, J. Wróbel, F. Kyrychenko, T. Wojtowicz, and S. Takeyama, App. Phys. Lett. **79**, 1789 (2001).

⁹ G. Cywiński, M. Czczcott, J. Wróbel, K. Fronc, A. Aleszkiewicz, S. Maćkowski, T. Wojtowicz, and J. Kossut, Physica E **13**, 560 (2002).

¹⁰ P. Redliński, T. Wojtowicz, T. G. Rappoport, A. Libál, J. K. Furdyna, and B. Jankó, submitted to Appl. Phys. Lett. (2004).

¹¹ J. K. Furdyna, J. Appl. Phys. **64**, R29 (1988).

¹² J. K. Furdyna and J. Kossut, *Diluted Magnetic Semiconductors* (Academic, Boston, 1988).

¹³ T. Dietl, M. Sawicki, M. Dahl, D. Heiman, E. D. Isaacs, M. J. Graf, S. I. Gubarev, and D. L. Alov, Phys. Rev. B **43**, 3154 (1991).

¹⁴ B. Kuhn-Heinrich, W. Ossau, H. Heinke, F. Fischer, T. Liz, A. Waag, and G. Landwehr, Applied Physics Letters **63**,

- 2932 (1993).
- ¹⁵ O. Madelung, *Introduction to Solid-State Theory* (Springer, New York, 1996), 3rd ed.
- ¹⁶ J. M. Luttinger and W. Kohn, Phys. Rev. **97**, 969 (1955).
- ¹⁷ M. Abolfath, T. Jungwirth, J. Brum, and A. H. MacDonald, Phys. Rev. B **63**, 054418 (2001).
- ¹⁸ J. D. Jackson, *Classical electrodynamics* (Wiley, New York, 1999), xxi ed.
- ¹⁹ B. Kuhn-Heinrich, W. Ossau, E. Bangert, A. Waag, and G. Landwehr, Solid State Communications **91**, 413 (1994).
- ²⁰ J. K. Ha, R. Hertel, and J. Kirschner, Phys. Rev. B **67**, 224432 (2003).
- ²¹ P. A. Crowell, V. Nikitin, D. D. Awschalom, F. Flack, N. Samarth, and G. A. Prinz, Journal of Applied Physics **81**, 5441 (1997).
- ²² M. J. Donahue and D. G. Porter, Interagency Report NISTIR 6376, National Institute of Standards and Technology (1999).
- ²³ F. Pulizzi, P. C. M. Christianen, J. C. Maan, T. Wojtowicz, G. Karczewski, and J. Kossut, Phys. Stat. Sol a **178**, 33 (2000).